Cavity Quantum Acoustic Device in the Multimode Strong Coupling Regime

Bradley A. Moores, Lucas R. Sletten, Jeremie J. Viennot, and K. W. Lehnert

Cavity quantum acoustic device in the multimode strong coupling regime

Bradley A. Moores,[*] Lucas R. Sletten,[†] Jeremie J. Viennot, and K. W. Lehnert

JILA, National Institute of Standards and Technology and the University of Colorado, Boulder, Colorado 80309, USA and
Department of Physics, University of Colorado, Boulder, Colorado 80309, USA
(Dated: March 12, 2018)

We demonstrate an acoustical analog of a circuit quantum electrodynamics system that leverages acoustic properties to enable strong multimode coupling in the dispersive regime while suppressing spontaneous emission to unconfined modes. Specifically, we fabricate and characterize a device that comprises a flux tunable transmon coupled to a $300\,\mu$m long surface acoustic wave resonator. For some modes, the qubit-cavity coupling reaches $6.5\,$MHz, exceeding the cavity loss rate ($200\,$kHz), qubit linewidth ($1.1\,$MHz), and the cavity free spectral range ($4.8\,$MHz), placing the device in both the strong coupling and strong multimode regimes. With the qubit detuned from the confined modes of the cavity, we observe that the qubit linewidth strongly depends on its frequency, as expected for spontaneous emission of phonons, and we identify operating frequencies where this emission rate is suppressed.

Emergent phenomena of many-body spin physics may be studied more readily with artificial systems rather than real materials. This possibility has led to a proliferation of techniques striving to emulate model Hamiltonians that exhibit many-body localization [1–4], topological protection [5, 6], and quantum phase transitions [7–9]. Of these artificial systems, transmon qubits coupled by microwave frequency electrical resonances show tremendous promise [10]. Specifically, if microwave excitations of the qubits or resonators are regarded as particles, the strong electrical non-linearity of the qubit creates an effective particle-particle interaction that is much larger than the relevant dissipation and decoherence processes [11]. Such an equivalently strong interaction has yet to be demonstrated with optical photons. Furthermore, in contrast to artificial systems that hold single atoms in optical lattices [12], planar circuits are rigidly fixed to their substrate and therefore have no spatial entropy.

Coupling many qubits to a dense cavity spectrum has been proposed as a means of engineering finite-range interactions for use in analog quantum simulations [13]. Such a system would consist of multiple degenerate qubits within a multimode cavity in the dispersive limit, where the qubits are detuned from the cavity by much more than the qubit-cavity coupling rate. However, building this in the circuit quantum electrodynamics (cQED) architecture [14–16] is hindered by the mismatch of scales between the qubits and the electromagnetic modes. For example, low dissipation planar resonators are centimeter long transmission lines [17], whereas the transmons are generally $\sim 100\,\mu$m. Furthermore these planar resonators are difficult to shield from each other, often resulting in undesired couplings.

As sound propagates 5 orders of magnitude slower than the speed of light, this scale mismatch can be overcome by replacing electromagnetic resonators with acoustic cavities, a strategy that has been pursued with bulk acoustic waves [18, 19]. Surface acoustic waves (SAWs) [20] have the additional feature that they are confined to the surface of a chip, allowing them to interact with sophisticated planar structures and many qubits. They readily make compact, multimode cavities with excellent shielding. At low temperatures and with excitations on the single phonon scale, SAW cavities have been demonstrated with high quality factors [21, 22]. Transmon qubits have been successfully coupled to propagating SAWs on GaAs [23], and to a single mode of a SAW resonator on quartz [24–26], but presently it's unclear what limits the coherence of acoustically coupled qubits. In order for qubits in cavity quantum acoustodynamical (CQAD) systems to experience coherent and finite range interactions, the system should operate in both the strong coupling and strong multimode limits.

In this Letter, we demonstrate such a CQAD system where the qubit-cavity coupling strength is larger than both the qubit and cavity decoherence rates, and also larger than the cavity free spectral range (FSR) ν_{FSR}. We also show that a qubit coupled to a SAW cavity has a special property that allows it to overcome an essential incompatibility between long qubit coherence and dispersive coupling to a multimode cavity [28]. In detail, when the qubit is resonant with the spectrum of acoustic modes, we observe clear avoided crossings and extract the couplings g_m of the qubit to 17 high quality modes of the acoustic cavity, finding $g_m/2\pi \sim \nu_{\mathrm{FSR}}$ for most modes. This strong multimode coupling inhibits the qubit from reaching the dispersive regime (detuned far from all cavity modes) when its frequency lies between these modes. However, the cavity confines phonons only over a narrow frequency range, allowing the qubit to be far detuned from all resonant modes while also relaxing the qubit via phonon radiation. Indeed, in the dispersive regime we measure the qubit linewidth as a function of qubit frequency and resolve a substantial contribution from spontaneous emission of unconfined phonons [29]. But crucial to the feasibility of many-body spin emulation, we also identify special qubit frequencies where this emission is prohibited.
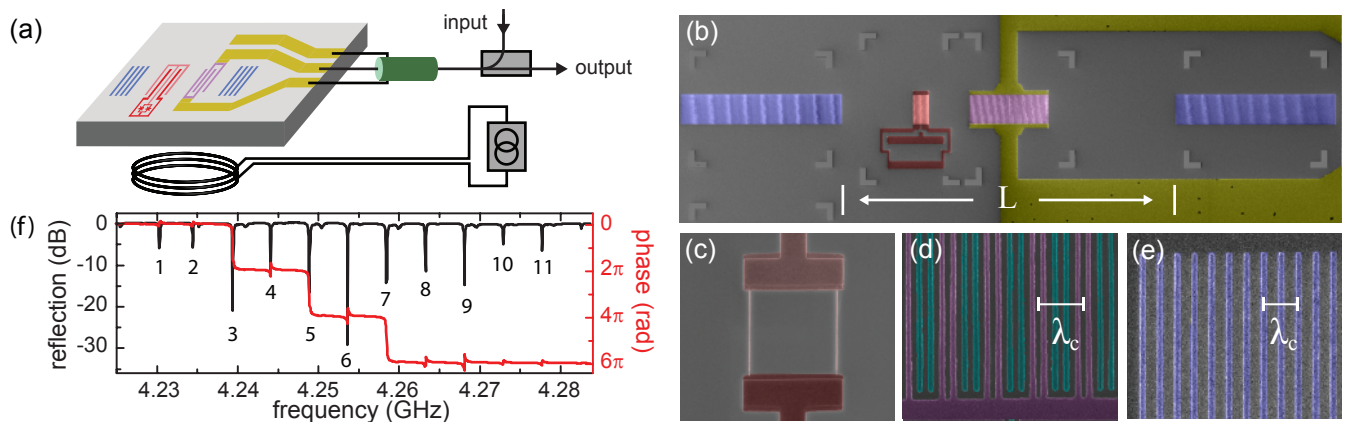
FIG. 1. Device diagram and acoustical cavity spectrum. (a) A cartoon schematic of the SAW cavity, acoustically coupled qubit, and the microwave network for control and measurement. (b) A false color SEM image of the fabricated device before the Josephson junction was patterned. Two Bragg reflectors (blue), each consisting of 400 Al strips, are spaced by $L = 275\,\mu\text{m}$ to define a SAW cavity, and a split-junction transmon qubit (red) was placed at $L_{\text{eff}}/4$ from the left reflector. A cavity-IDT (pink) with 125 periods at $L/2$ is used to drive and readout the cavity modes. The center- and ground-conductor of a coplanar waveguide (yellow) contact either side of the IDT. Measurements consist of detecting the reflection of a microwave tone applied to the cavity-IDT. A directional coupler separates incident and reflected waves, so that the reflected signal is passed through a high electron mobility transistor (HEMT) amplifier and measured. False color SEM images of (c) a split Josephson-junction with a $7{\times}7\,\mu\text{m}^2$ loop area, (d) a split-finger IDT with the upper electrode in green and the lower in purple [27], and (e) several Al stripes within a Bragg reflector. The characteristic wavelength of the cavity is indicated, $\lambda_c = v_s/f_c = 677\,\text{nm}$, where the center frequency is $f_c = 4.253\,\text{GHz}$. (f) A microwave reflection measurement of the SAW cavity reveals 11 (numbered) prominent longitudinal modes within the mirror bandwidth.

We demonstrate these characteristics with the device drawn schematically in Fig. 1(a) and imaged in Fig. 1(b). This device is a flux tunable qubit inside a multimode SAW cavity on GaAs. The qubit is a transmon consisting of a split Josephson junction in parallel with a split-finger interdigitated transducer (IDT) [27]. The IDT forms both a shunting capacitor ($\sim$100 fF) and a piezoelectric transducer that interacts with SAW waves. The cavity is defined by two Bragg reflectors separated by $275\,\mu\text{m}$, each consisting of a periodic array of aluminum stripes. Each stripe weakly reflects incoming SAWs ($<$2%), primarily due to mass loading [30]. The arrays are highly reflective over a narrow frequency range ($\sim$50 MHz), while SAW penetration makes the effective cavity length $L_{\text{eff}} = 300\,\mu\text{m}$. The acoustic response is probed through a split-finger IDT, centered in the cavity, that converts between mechanical excitations in the cavity and microwave signals in the coplanar waveguide.

We first characterize the acoustic modes by tuning the transmon far away from the cavity resonances using an off-chip coil. The device was embedded in a microwave measurement network as shown in Fig. 1(a) and cooled below 30 mK in a dilution refrigerator. Fig. 1(f) shows the microwave reflection coefficient versus frequency of the acoustic cavity. Over the mirror bandwidth of approximately 50 MHz, we observe 11 prominent equally spaced resonances. For each of these dips, there are weaker adjacent resonances at higher frequency. We in-

terpret the 11 prominent resonances as purely longitudinal cavity modes, and the higher frequency satellites as modes with a non-zero transverse mode number. In what follows, we will model the 11 longitudinal modes and the 6 more visible transverse modes. From the spacing between longitudinal modes we extract the cavity FSR $\nu_{\text{FSR}} = v_s/2L_{\text{eff}} = 4.8\,\text{MHz}$, where $v_s = 2880\,\text{m/s}$ is the speed of sound on GaAs, consistent with our expectation from the cavity geometry. The longitudinal modes have $\kappa_l/2\pi \approx 200\,\text{kHz}$ linewidths, and the transverse mode linewidths are slightly lossier with $\kappa_t/2\pi \approx 400\,\text{kHz}$.

Having characterized the bare cavity spectrum, we tune the qubit into resonance with the modes to measure the transmon-cavity coupling strengths. Figure 2(a) shows the cavity response as the coil current is swept, revealing two sets of avoided crossings at $\pm 0.27\,\Phi/\Phi_0$. The qubit position in the cavity has significant consequences on the spectrum as the coupling strengths g_m depend on the spatial overlap of a mode and the qubit-IDT fingers. For example, the transmon couples strongest to modes that have anti-nodes aligned with the qubit-IDT fingers. Zooming into a single set of avoided crossings (Fig. 2b) reveals that the transmon indeed couples to the cavity modes with varying strength.

Although the spectrum looks complicated, the longitudinal mode couplings exhibit a simple oscillating pattern. For example, modes 4 and 8 strongly couple, modes 2, 6, and 10 barely couple, and the odd modes all mod-
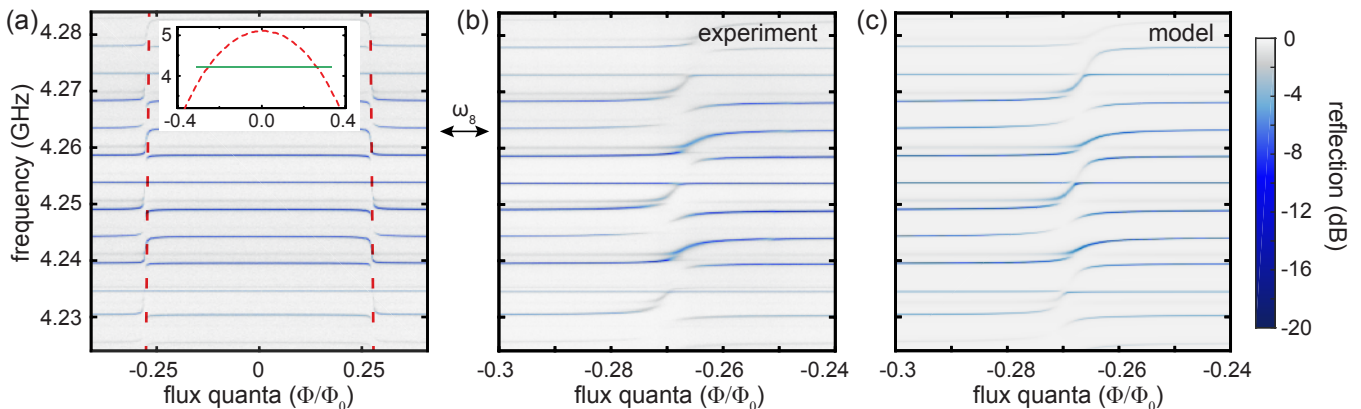
FIG. 2. Resonantly coupled multimode CQAD system. (a) The plot shows the cavity reflection (color scale) as the transmon is tuned by varying the applied magnetic flux. The red dashed line indicates the transmon's flux dependent resonance. The inset shows the expected qubit frequency (red), which has a maximum at 5.08 GHz. The green section indicates the measured range of panel (a). (b) Zoom in on the first set of avoided crossings shown in panel (a). (c) A model for the acoustic spectrum based on the interaction Hamiltonian, Eq. (2).

erately couple. The qubit position at $L_{\mathrm{eff}}/4$ creates a mode-dependent coupling strength

$$g_m = g_0 \sin\left(\frac{\pi}{4}m + \phi_q\right) \qquad (1)$$

where g_0 is an overall coupling strength that is sinusoidally modulated by a four mode period, and ϕ_q is an overall phase shift set by the small deviation in the qubit position from $L_{\mathrm{eff}}/4$. Coupling to the transverse modes can be written in a similar way, with the same phase ϕ_q and a smaller g_0 which can be approximated from the cavity-IDT spectrum [27].

Using this insight, we make a simple model of the 17 modes that detectably hybridize with the qubit. Coupling between the multimode cavity and qubit can be described by an 18×18 interaction Hamiltonian

$$H/\hbar = \begin{pmatrix} \omega_1 & & & g_1 \\ & \omega_2 & & g_2 \\ & & \ddots & \vdots \\ g_1 & g_2 & \cdots & \omega_{\mathrm{q}} \end{pmatrix} \qquad (2)$$

where $\omega_k/2\pi$ are the 17 uncoupled cavity modes (11 longitudinal and 6 transverse), and $\omega_{\mathrm{q}}/2\pi$ is the qubit ground to first excited state transition frequency. The number of coupling terms, and consequently fit parameters, can be significantly reduced from 17 to 3 using Eq. (1) and an equivalent equation for the transverse modes. We diagonalize the Hamiltonian as a function of the qubit frequency to obtain the hybridized modes [27]. We found the optimum fit is $g_0/2\pi = 6.5\,\mathrm{MHz}$ and $\phi_q = \pi/2 - 0.07\,\mathrm{rad}$, which is plotted in Fig. 2(c). The model indicates that modes 4 and 8 couple strongest to the transmon with $g_{4,8}/2\pi = 6.48\,\mathrm{MHz}$. Because coupling strength of some modes exceed the cavity FSR

($\nu_{FSR} = 4.8\,\mathrm{MHz}$), the device seems to operate in the strong multimode regime.

The hallmark of the strong multimode limit consists of many modes hybridizing with each other through a mutual qubit coupling, while the qubit participation in each eigenmode remains low [31]. We can use our model Hamiltonian to infer that our device operates in this limit. In Fig. 3(a) we plot the qubit and acoustic mode participation in an eigenstate as the qubit frequency varies with magnetic field. On resonance, three modes strongly hybridize, where each mode almost equally contributes to the eigenvalue, while the qubit participation remains small (<7%). Fig. 3(b) shows agreement between the data and model for the hybridization shown in Fig. 3(a).

Because the qubit participation is low, the well resolved avoided crossings do not imply that the CQAD system reaches the strong coupling limit ($g_0 > \{\kappa,\gamma\}$). To show that it does, we measure the qubit linewidth by operating the device in the dispersive limit [32]. We begin by detuning the qubit far from all of the cavity resonances (by at least $100\,\mathrm{MHz} \gg g_0/2\pi$), which is possible because the mirrors that define the cavity are narrowband (Fig. 1f). We then apply two tones to the cavity-IDT, one resonant with the eighth longitudinal mode of the cavity and one nearly resonant with the qubit. By monitoring the reflection of the tone at ω_8, while varying the frequency and power of the qubit drive we detect the qubit's resonance through the qubit-state-dependent dispersive shift χ of the cavity resonance.

Using this dispersive measurement of the qubit's state, we flux tune the qubit's resonance frequency and verify that our CQAD system behaves according to a generalized Jaynes-Cummings Hamiltonian. Specifically, at each value of applied flux, we measure the qubit frequency
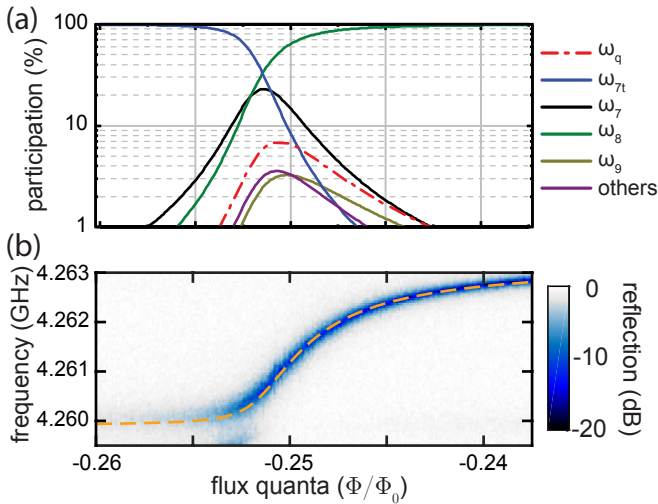
FIG. 3. Hybridization of modes in the strong multimode regime. (a) The solid lines show the squared coefficients of the eigenvector (participation) in the uncoupled mode basis as the qubit tunes with magnetic field. At -0.252 flux quanta, longitudinal modes ω_7 and ω_8 and transverse mode ω_{7t} nearly equally contribute to 89% of the eigenvector. The 'others' trace shows the combined contribution of the remaining modes. (b) The acoustic spectrum (from Fig. 2b) between modes ω_7 and ω_8. The dotted line shows the eigenvalue fit from the model corresponding to the superposition of modes from (a).

FIG. 4. Measurements in the dispersive regime. (a) The dispersive shift of cavity mode ω_8 versus qubit frequency (ω_q). The purple, orange, and blue dashed lines indicate $\omega_8/2\pi$, $\omega_8/2\pi+\alpha$, and $\omega_8/2\pi+3\alpha/2$ respectively, where $\alpha = 273\,\mathrm{MHz}$ is the transmon's anharmonicity [27]. The green line shows a prediction from the standard transmon model, and the solid blue line shows a prediction from diagonalizing a generalized Jaynes-Cummings Hamiltonian with a 4-level transmon. (b) The qubit linewidth versus qubit frequency. Red points are measurements, and the blue line shows the expected spontaneous emission rate of the qubit into SAWs based on the qubit-IDT geometry, with an offset to account for the intrinsic decoherence; i.e. processes other than spontaneous emission that decohere the qubit. The green region indicates the mirror bandwidth.

shift as function of cavity drive power (Stark shift). In the low power limit the Stark shift is linear with phonon number, with a slope of 2χ [27, 33]. Figure 4(a) compares χ measurements of the CQAD device to predictions from two models. When $\omega_q < \omega_8$, our transmon is well described by the standard transmon dispersive model [32], which only takes the lowest three energy levels into account and ignores two-phonon transitions. We use this regime to calibrate the single phonon power level. When $\omega_q > \omega_8$ and a large phonon occupation is used, other transition frequencies and higher order effects become significant. To take these effects into account, we model the dispersive shift by diagonalizing a generalized Jaynes-Cummings Hamiltonian consisting of a 4-level transmon and a harmonic oscillator truncated at 50 excitations [27].

With qubit spectroscopy well modeled by transmon theory, we can use the qubit linewidth measured in the low power limit of the cavity and qubit drives as an upper bound on the qubit decoherence rate. Unlike a system where a cavity fully encloses a qubit [34], the CQAD device interacts with unconfined modes outside of the mirror bandwidth that could limit the qubit coherence. However, the qubit transition can be tuned to specific frequencies in which the emission can be strongly suppressed. The spatial periodicity and finite length of the qubit-IDT combine to emit SAWs with wavelengths centered around λ_c. In the frequency domain, the IDT's spatial periodicity yields a SAW emission rate with a $\sin^2 X/X^2$ frequency dependence, where $X = N_q\pi(f-f_c)/f_c$ and N_q is the number of qubit-IDT finger periods [27]. This spectrum consists of evenly spaced minima where emission is prohibited due to coherent cancellation. The blue curve in Fig. 4(b) shows the expected qubit linewidth as a sum of the predicted spontaneous phonon emission rate of the transmon and a constant offset to account for intrinsic decoherence. We measure the linewidth as a function of qubit drive power and extrapolate to zero power to infer the qubit decoherence rate, shown as red data points. The qubit linewidth narrows when its frequency is within an IDT band minima (e.g. 3.9 GHz), and broadens by up to a factor of 3 near a maximum (e.g. 4.0 GHz). From the offset between the predicted IDT spontaneous emission rate and the observed qubit linewidth, we estimate an upper-bound on the intrinsic qubit linewidth of $\gamma/2\pi = 1.1\,\mathrm{MHz}$. Thus, the qubit can exchange energy with a SAW mode at a rate about 6 times greater than its intrinsic decoherence rate, reaching the strong coupling limit.

In conclusion, we have shown that superconducting qubits and SAW cavities can reach the strong coupling

and multimode regimes of CQAD while avoiding an incompatibility between qubit coherence times and dispersive operation. Although emulating many-body spin systems will require further improvement in qubit coherence, we show that decoherence from phonon emission can be strongly suppressed. There are multiple prospects to move deeper into the strong coupling regime, including use of a stronger piezoelectric substrate and surface treatment to reduce loss in metal-surface interfaces. Future work could use SAW coupled transmons to coherently exchange quantum states between atom-like defects or quantum dots and superconducting qubits, as proposed in some schemes to create a quantum electro-optical converter [35]. Finally, with recent progress in improving the coherence of nano-mechanical resonators [36], these may supplant electromagnetic resonators in certain quantum information processing tasks, particularly where size and isolation are high priorities.

* These two authors contributed equally; bradley.moores@colorado.edu
† These two authors contributed equally

[1] R. Dalichaouch, J. P. Armstrong, S. Schultz, P. M. Platzman, and S. L. McCall, Nature **354**, 53 (1991).
[2] D. S. Wiersma, P. Bartolini, A. Lagendijk, and R. Righini, Nature **390**, 671 (1997).
[3] J. E. Lye, L. Fallani, M. Modugno, D. S. Wiersma, C. Fort, and M. Inguscio, Phys. Rev. Lett. **95**, 10 (2005).
[4] C. Fort, L. Fallani, V. Guarrera, J. E. Lye, M. Modugno, D. S. Wiersma, and M. Inguscio, Phys. Rev. Lett. **95**, 1 (2005).
[5] C. Y. Lu, W. B. Gao, O. Gühne, X. Q. Zhou, Z. B. Chen, and J. W. Pan, Phys. Rev. Lett. **102**, 1 (2009).
[6] M. C. Rechtsman, J. M. Zeuner, Y. Plotnik, Y. Lumer, D. Podolsky, F. Dreisow, S. Nolte, M. Segev, and A. Szameit, Nature **496**, 196 (2013).
[7] M. Greiner, O. Mandel, T. Esslinger, T. W. Ha, and I. Bloch, Nature **415**, 39 (2002).
[8] P. Roushan, C. Neill, A. Megrant, Y. Chen, R. Babbush, R. Barends, B. Campbell, Z. Chen, B. Chiaro, A. Dunsworth, A. Fowler, E. Je, J. Kelly, E. Lucero, J. Mutus, P. J. J. O. Malley, M. Neeley, C. Quintana, D. Sank, A. Vainsencher, J. Wenner, T. White, E. Kapit, and H. Neven, Nature Phys. **13**, 146 (2017).
[9] M. Fitzpatrick, N. M. Sundaresan, A. C. Li, J. Koch, and A. A. Houck, Phys. Rev. X **7**, 1 (2017).
[10] A. A. Houck, H. E. Türeci, and J. Koch, Nature Phys. **8**, 292 (2012).
[11] S. Schmidt and J. Koch, Ann. der Phys. **525**, 395 (2013).
[12] A. Goban, C. L. Hung, J. D. Hood, S. P. Yu, J. A. Muniz, O. Painter, and H. J. Kimble, Phys. Rev. Lett. **115**, 1 (2015).
[13] P. Strack and S. Sachdev, Phys. Rev. Lett. **107**, 1 (2011).
[14] A. Wallraff, D. Schuster, A. Blais, L. Frunzio, R. Huang, J. Majer, S. Kumar, S. Girvin, and R. Schoelkopf, Nature **431**, 162 (2004).
[15] A. Blais, R. S. Huang, A. Wallraff, S. M. Girvin, and R. J. Schoelkopf, Phys. Rev. A **69**, 062320 (2004).
[16] D. C. McKay, R. Naik, P. Reinhold, L. S. Bishop, and D. I. Schuster, Phys. Rev. Lett. **114**, 1 (2015).
[17] L. Frunzio, A. Wallraff, D. Schuster, J. Majer, and R. Schoelkopf, Appl. Supercond. **15**, 860 (2005).
[18] A. D. O'Connell, M. Hofheinz, M. Ansmann, R. C. Bialczak, M. Lenander, E. Lucero, M. Neeley, D. Sank, H. Wang, M. Weides, J. Wenner, J. M. Martinis, and A. N. Cleland, Nature **464**, 697 (2010).
[19] Y. Chu, P. Kharel, W. Renninger, L. Burkhart, L. Frunzio, P. Rakich, and R. Schoelkopf, Science **1511**, 1 (2017).
[20] C. Campbell, *Surface acoustic wave devices and their signal processing applications* (Academic Press, 1989) p. 470.
[21] E. B. Magnusson, B. H. Williams, R. Manenti, M. S. Nam, a. Nersisyan, M. J. Peterer, a. Ardavan, and P. J. Leek, Appl. Phys. Lett. **106**, 4 (2015).
[22] R. Manenti, M. J. Peterer, A. Nersisyan, E. B. Magnusson, A. Patterson, and P. J. Leek, Phys. Rev. B **93**, 1 (2016).
[23] M. V. Gustafsson, T. Aref, A. F. Kockum, M. K. Ekstrom, G. Johansson, and P. Delsing, Science **346**, 207 (2014).
[24] R. Manenti, A. F. Kockum, A. Patterson, T. Behrle, J. Rahamim, G. Tancredi, F. Nori, and P. J. Leek, Nature Comm. **8**, 1 (2017).
[25] A. Noguchi, R. Yamazaki, Y. Tabuchi, and Y. Nakamura, arXiv:1710.00467.
[26] A. N. Bolgar, J. I. Zotova, D. D. Kirichenko, I. S. Besedin, A. V. Semenov, R. S. Shaikhaidarov, and O. V. Astafiev, arXiv:1710.06476.
[27] See Supplementary Information for details.
[28] A. Blais, J. Gambetta, A. Wallraff, D. I. Schuster, S. M. Girvin, M. H. Devoret, and R. J. Schoelkopf, Phys. Rev. A **75**, 1 (2007).
[29] A. F. Kockum and P. Delsing, Phys. Rev. A **90**, 1 (2014).
[30] S. Datta, *Surface acoustic wave devices* (Prentice-Hall, 1986).
[31] N. M. Sundaresan, Y. Liu, D. Sadri, L. J. Szcs, D. L. Underwood, M. Malekakhlagh, H. E. Türeci, and A. A. Houck, Phys. Rev. X **5**, 021035 (2015).
[32] J. Koch, T. M. Yu, J. Gambetta, A. A. Houck, D. I. Schuster, J. Majer, A. Blais, M. H. Devoret, S. M. Girvin, and R. J. Schoelkopf, Phys. Rev. A **76**, 1 (2007).
[33] D. I. Schuster, A. Wallraff, A. Blais, L. Frunzio, R. S. Huang, J. Majer, S. M. Girvin, and R. J. Schoelkopf, Phys. Rev. Lett. **94**, 1 (2005).
[34] H. Paik, D. I. Schuster, L. S. Bishop, G. Kirchmair, G. Catelani, A. P. Sears, B. R. Johnson, M. J. Reagor, L. Frunzio, L. I. Glazman, S. M. Girvin, M. H. Devoret, and R. J. Schoelkopf, Phys. Rev. Lett. **107**, 1 (2011).
[35] M. J. A. Schuetz, E. M. Kessler, G. Giedke, L. M. K. Vandersypen, M. D. Lukin, and J. I. Cirac, Phys. Rev. X **5**, 1 (2015).
[36] S. M. Meenehan, J. D. Cohen, G. S. Maccabe, F. Marsili, M. D. Shaw, and O. Painter, Phys. Rev. X **5**, 1 (2015).